# Multimodal data integration for biologically-relevant artificial intelligence to guide adjuvant chemotherapy in stage II colorectal cancer

Chenyi Xie,[a,b,c,g] Ziyu Ning,[c,d,g] Ting Guo,[c] Lisha Yao,[c] Xiaobo Chen,[b] Wanghong Huang,[c] Suyun Li,[b] Jiahui Chen,[b] Ke Zhao,[a,b,c] Xiuwu Bian,[e] Zhenhui Li,[f] Yanqi Huang,[b] Changhong Liang,[b] Qingling Zhang,[c,d,**] and Zaiyi Liu[a,b,c,*]

[a]Guangdong Cardiovascular Institute, Guangdong Provincial People's Hospital (Guangdong Academy of Medical Sciences), Guangzhou, 510080, China
[b]Department of Radiology, Guangdong Provincial People's Hospital (Guangdong Academy of Medical Sciences), Southern Medical University, Guangzhou, 510080, China
[c]Guangdong Provincial Key Laboratory of Artificial Intelligence in Medical Image Analysis and Application, Guangzhou, 510080, China
[d]Department of Pathology, Guangdong Provincial People's Hospital (Guangdong Academy of Medical Sciences), Southern Medical University, Guangzhou, Guangdong, 510080, China
[e]Institute of Pathology and Southwest Cancer Center, Southwest Hospital, Third Military Medical University (Army Medical University) and Key Laboratory of Tumor Immunopathology, Ministry of Education of China, Chongqing, 400038, China
[f]Department of Radiology, The Third Affiliated Hospital of Kunming Medical University, Yunnan Cancer Hospital, Kunming 650000, China

eBioMedicine
2025;117: 105789
Published Online xxx
https://doi.org/10.1016/j.ebiom.2025.105789

## Summary

**Background** Adjuvant chemotherapy provides a limited survival benefit (<5%) for patients with stage II colorectal cancer (CRC) and is suggested for high-risk patients. Given the heterogeneity of stage II CRC, we aimed to develop a clinically explainable artificial intelligence (AI)-powered analyser to identify radiological phenotypes that would benefit from chemotherapy.

**Methods** Multimodal data from patients with CRC across six cohorts were collected, including 405 patients from the Guangdong Provincial People's Hospital for model development and 153 patients from the Yunnan Provincial Cancer Centre for validation. RNA sequencing data were used to identify the differentially expressed genes in the two radiological clusters. Histopathological patterns were evaluated to bridge the gap between the imaging and genetic information. Finally, we investigated the discovered morphological patterns of mouse models to observe imaging features.

**Findings** The survival benefit of chemotherapy varied significantly among the AI-powered radiological clusters [interaction hazard ratio (iHR) = 5.35, (95% CI: 1.98, 14.41), adjusted $P_{interaction}$ = 0.012]. Distinct biological pathways related to immune and stromal cell abundance were observed between the clusters. The observation only (OO)-preferable cluster exhibited higher necrosis, haemorrhage, and tortuous vessels, whereas the adjuvant chemotherapy (AC)-preferable cluster exhibited vessels with greater pericyte coverage, allowing for a more enriched infiltration of B, $CD4^+$-T, and $CD8^+$-T cells into the core tumoural areas. Further experiments confirmed that changes in vessel morphology led to alterations in predictive imaging features.

**Interpretation** The developed explainable AI-powered analyser effectively identified patients with stage II CRC with improved overall survival after receiving adjuvant chemotherapy, thereby contributing to the advancement of precision oncology.

**Funding** This work was funded by the National Science Fund of China (81925023, 82302299, and U22A2034), Guangdong Provincial Key Laboratory of Artificial Intelligence in Medical Image Analysis and Application (2022B1212010011), and High-level Hospital Construction Project (DFJHBF202105 and YKY-KF202204).

*Corresponding author. Guangdong Provincial People's Hospital (Guangdong Academy of Medical Sciences), Southern Medical University, 106 Zhongshan 2nd Road, Guangzhou, 510080, China.
**Corresponding author. Guangdong Provincial People's Hospital (Guangdong Academy of Medical Sciences), Southern Medical University, 106 Zhongshan 2nd Road, Guangzhou, 510080, China.
*E-mail addresses:* liuzaiyi@gdph.org.cn (Z. Liu), zhangqingling@gdph.org.cn (Q. Zhang).
[g]Contributed equally to this work as first authors.

Keywords: Stage II colorectal cancer; Predictive biomarker; Multimodal artificial intelligence; Imaging; Prognosis; Risk stratification

## Research in context

### Evidence before this study

We searched PubMed for relevant articles about explainability artificial intelligence (AI) published from database inception to 15 November 2024 using the search terms "deep learning" OR "artificial intelligence" OR "machine learning" OR "radiomics" AND "colorectal cancer" AND "explainability" OR "biologic basis". Only two machine learning-based studies utilising computed tomography (CT) images have been published in the context of predicting clinical outcomes in colorectal cancer (CRC), with a particular focus on identifying underlying biological pathways. However, these studies have primarily focused on identifying prognostic biomarkers for patients with CRC, which are less relevant for post-operative treatment planning, especially for stage II CRC. Additionally, the investigation of the underlying biological pathways focused on radiogenomic analysis, with limited validation conducted at the histopathological level. No studies have reported preclinical experiments to validate the alterations in predictive imaging features observed in CRC, leaving a critical gap in the translation of imaging biomarkers into clinical applications.

### Added value of this study

The developed AI-powered tumour detection and risk stratification model performed well in identifying patients with stage II CRC with a favourable prognosis after receiving adjuvant chemotherapy. Radiological stratification could potentially reduce the morbidity and economic costs associated with current stage II CRC management by avoiding overtreatment and identifying missed cases that are suitable for adjuvant treatment. Second, in response to concerns regarding the black-box nature of AI, we integrated multi-omics data from six CRC cohorts and preclinical animal experiments to gain a comprehensive understanding of the biological heterogeneity of imaging subtypes, proposing an explainability approach to engender trust in AI decisions.

### Implications of all the available evidence

This study takes a step toward closing the knowledge gap between radiographic patterns and gene expression by incorporating histopathological features to confirm the consistency of radiogenomic findings at the cellular scale. Distinct vessel stroma-related histopathological patterns and transcriptomic profiles were observed among the radiological clusters of CRC, which could potentially affect the effectiveness of chemotherapy. Furthermore, this study verified that interventions on vessel patterns in preclinical settings can be reflected in textural heterogeneity. This increases the transparency and acceptance of our AI-based imaging model, which will affect clinical decisions in treating patients with stage II CRC.

## Introduction

Fluoropyrimidine or oxaliplatin doublet adjuvant chemotherapy is considered an option for high-risk stage II colorectal cancer (CRC), but the usefulness of adjuvant chemotherapy remains controversial.[1] Adjuvant chemotherapy provides only a modest 5-year survival benefit (<5%)[2] and should be administered with caution.[3,4] Considering the underlying complications of intratumoural heterogeneity, risk determination is crucial for guiding therapeutic decisions in these patients. The widespread utilisation of complex molecular biomarkers is susceptible to limitations resulting from the dynamic and heterogeneous nature of cancer cells and invasiveness of the tissue sampling procedure. Recently, the development of artificial intelligence (AI) and radiomics applications in radiology has provided technological feasibility for subtyping patients with heterogeneous CRC.[5,6] However, most studies have focused on determining prognostic biomarkers, which are less important for post-operative therapy planning. Validated predictive biomarkers using noninvasive imaging are needed to identify patients with stage II CRC with a favourable prognosis after receiving adjuvant chemotherapy.

The process of establishing AI models is often purely data-driven, and there are risks of overfitting or over-interpretation of the constructed models.[7] Lack of explanation from the biomedical aspect causes concern over "black box" decisions. Efforts to reintroduce the biological relevance of radiological features have gained momentum in this field. These approaches include the integration of genomic correlates and the evaluation of microscopic histopathological marker expression. Radiogenomics has been used to investigate the correlations between radiological features and meaningful biological activities.[8] Exploring the genetic and molecular characteristics of tumours and microenvironments corresponding to radiomics-based biomarkers can substantially change the clinical management of CRC. Histopathological findings can further verify the consistency of radiogenomic findings on a cellular scale, bridging the gap between imaging and genetic information.[9–11] However, the acceptance of

radiogenomics remains limited owing to the lack of causality. To address this concern, researchers have endeavoured to substantiate the biological significance of imaging features in animal models. Panth et al.[12] reported that radiomics quantifies the early effects of radiation treatment and genetic changes in cell line-derived xenograft models. Zinn et al.[13] reported that radiomic texture features could predict the POSTN status in POSTN-knockdown orthotopic xenograft mice. These results provided in-depth and robust insights into the biological foundations underlying the observed findings.

Therefore, our multicentre study aimed to identify AI-driven radiological phenotypes of stage II resected CRCs with a favourable prognosis after receiving adjuvant chemotherapy. We further analysed the genetic and histopathological profiles of the radiological subtypes to elucidate the biological basis of why and how radiological subtypes correlate with the survival benefits of adjuvant chemotherapy in CRC. Finally, the correlative linkages between imaging and biological characteristics were explored in preclinical settings with interventions to validate the observed correlations.

## Methods

### Ethics

This study was approved by the institutional review boards of the participating institutions (KY-N-2021-060-01). The requirement for informed patient consent was waived because of the retrospective nature of the study. Animal experiments were performed in strict accordance with the recommendations of the Guide for the Care and Use of Laboratory Animals of the South China University of Technology.

### Study population, data collection and clinical follow-up

Patients from Guangdong Provincial People's Hospital (GDPH) and Yunnan Provincial Cancer Centre (YNCC) were retrospectively included in the development and validation datasets of the AI-Power risk stratification analyser for chemotherapeutic benefit prediction (Fig. 1). For patients with no documented clinical endpoints, survival was censored on 28 February 2023 with a minimum 5-year follow-up. Inclusion criteria were: (a) patients had histopathologically confirmed stage II colon or rectal adenocarcinoma (histopathologically staged as T3 or T4, N0, M0, American Joint Committee on Cancer 8th edition) and had undergone surgical resection; (b) patients had received standard adjuvant chemotherapy or patients had not received any treatment after the completion of radical surgery; (c) individuals had undergone a diagnostic workup abdominal contrast-enhanced computed tomography (CT) scan within two weeks before surgery; and (d) the availability of comprehensive histological and clinical follow-up data. The exclusion criteria were as follows: (a) patients who had received radiotherapy, chemotherapy, or surgery for CRC before surgery; (b) individuals with a history of cancer or concurrent malignancies; and (c) patients with incomplete clinical, radiological, or pathological information. Four cohorts obtained from publicly available databases were included in this study. The Cancer Imaging Archive (COAD) cohort included diagnostic CT scans, chemotherapy information, and genomic data. Three additional public datasets accessed from the Gene Expression Omnibus (GEO) were collected as drug-associated datasets. Patients were treated with fluorouracil-based chemotherapy as part of the therapeutic regimen, regardless of whether they were receiving adjuvant or in progression, and their responses to chemotherapy were recorded. Sex was included as a biological variable due to its potential association with CRC outcomes.

### Image processing pipeline for the discovery of treatment decision-related subtypes

All patients underwent enhanced abdominal CT. Pretreatment contrast-enhanced CT images with 1.25-mm slices were retrieved from the Picture Archiving and Communication System and served as the primary imaging input for radiomic analysis. All patient-identifiable metadata were removed from DICOM files prior to analysis. DeepCRC,[14] a topology-aware deep-learning-based approach for automated colorectal and CRC segmentation, was used to delineate regions of interest covering the entire tumour in all slices. The pipeline of the DeepCRC segmentation method is provided in Supplementary Fig. S1. Tumour delineation covered the entire tumour in all slices in the presence of a primary lesion. Two experienced radiologists manually checked and validated the tumoural regions of interest (ROIs) using ITK-SNAP software. Discrepancies were resolved by consensus. The revised 3D ROI masks via DeepCRC were used as input for imaging feature extraction.

### Feature extraction, feature selection and model construction

Radiomic features were extracted from the original and wavelet-filtered images using PyRadiomics.[15] The image intensities were binned by 25 HU, and the voxel array shift was set to 1000. The defined radiomic features from the original and wavelet-filtered images were extracted. The original images depict baseline structural characteristics. Wavelet filtration (high-pass filter and low-pass filter) filtered the original images directionally in the x, y, and z directions, respectively, yielding eight different combinations of decompositions. These filtrations captured detailed disruptions in different orientations. The extracted radiomics features were divided into three groups: (I) first-order statistics (II) shape features, and (III) second-order features. Features defined below were in accord with feature definitions as described by the Imaging Biomarker Standardization

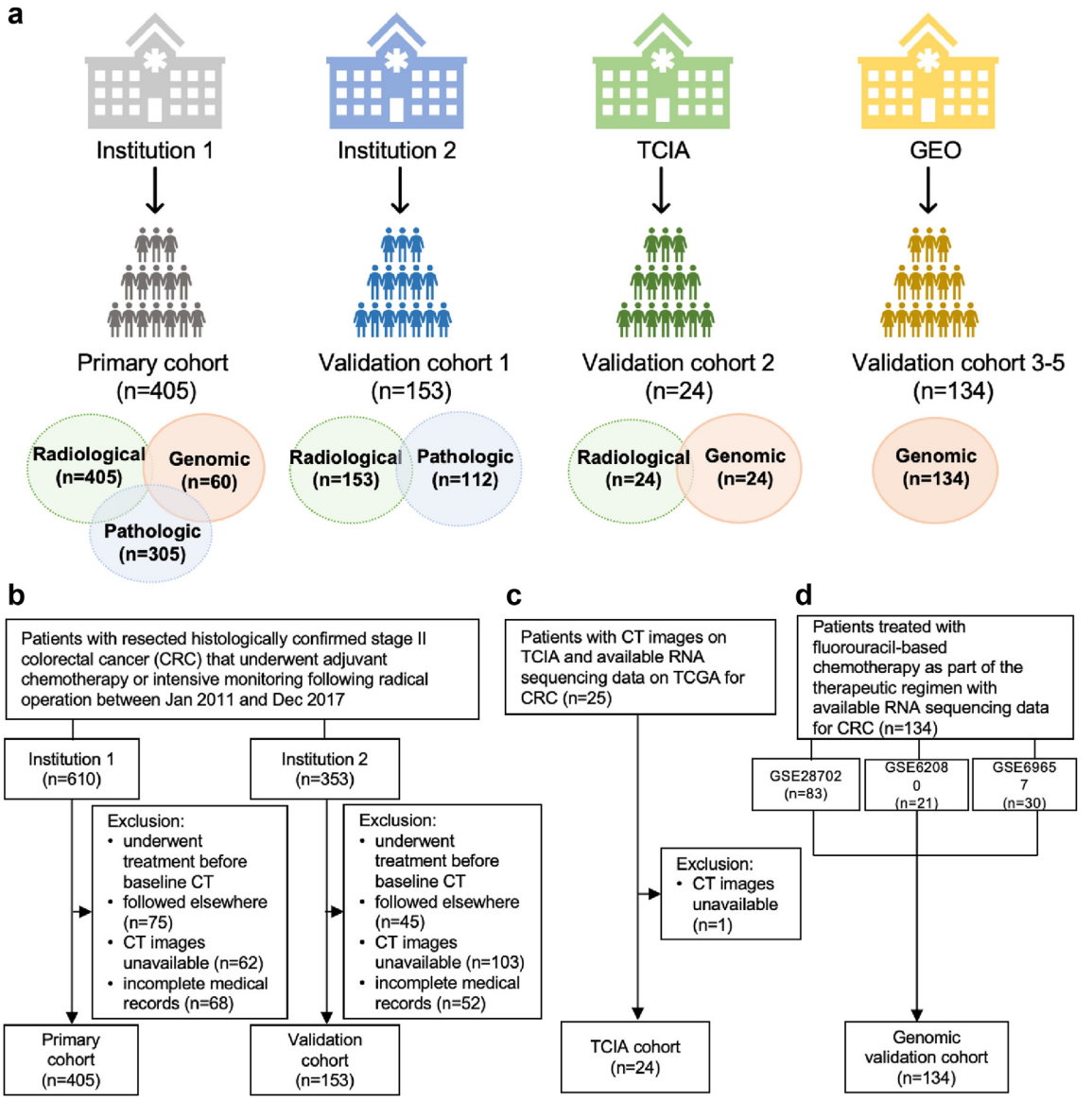


***Fig. 1:*** **Patient recruitment**. (a) Schematic illustration. (b) Development and validation cohorts. (c) TCIA cohort. (d) GEO cohorts. Abbreviations: CRC, colorectal cancer; TCIA, The Cancer Imaging Archive; GEO, Gene Expression Omnibus.

Initiative (IBSI). Detailed calculations of radiomics features are described and provided in online documentation of PyRadiomics (https://pyradiomics.readthedocs.io/en/latest/features.html). We conducted a test-retest study in a subset of 30 patients using original radiologist-contoured segmentations and automated radiologist-checked segmentations. Feature robustness was evaluated by intraclass correlation coefficients (ICC) of all radiomics features between different acquisition parameters, accounting for resampled voxels and slice spacing at a threshold value of 0.80.

Imaging features indicating treatment-specific survival benefits were selected using an interaction term (interaction hazard ratio, iHR) between treatment and survival status.[16] First, an interaction test is performed individually for each radiomic feature to assess the relationship between treatment and radiomic characteristics, and a subset of the most significant radiomic features is chosen. In particular, for a given radiomic feature, a standard multivariate Cox proportional hazards model is typically applied:

$$h_i(t) = h_0(t)exp\{\psi_1 r_i + \psi_2 x_i + \psi_3 r_i x_i\} \quad (1)$$

where $h_i(t)$ represents the baseline hazard, $\psi$ indicates the regression parameters, and $r_i$ indicates the treatment assignment for patient $i$, where $r_i$ corresponds the application status of chemotherapy. The product $r_i x_i$

represents the interaction between treatment and the radiomic feature value.

The selection of biomarkers was based on the Wald test statistic, for testing a null interaction effect ($\psi_3 = 0$). A standardized test statistic, $z$, which approximately followed a standard normal distribution under the null hypothesis of no interaction effects, was calculated as:

$$z = \frac{iHR}{se(iHR)} \quad (2)$$

where $iHR$ indicates for interaction-hazard ratio derived from the interaction term of Eq. (1). Features with $z$-statistics below 0.05 were selected for model construction.

Hierarchical clustering, an unsupervised clustering method, was employed to identify robust radiological phenotypes, offering a more unbiased approach to subtype discovery. The optimal number of clusters was determined using dendrogram and silhouette methods. This stratification provides a biomarker-driven framework to guide chemotherapy: adjuvant chemotherapy (AC)-preferable cluster and observation only (OO)- preferable cluster.

For the model evaluation, we conducted multiple comparisons to mitigate the risk of Type I errors for post-hoc analyses involving multiple markers across different risk subgroups. Specifically, we applied the Benjamini-Hochberg false discovery rate (FDR) method (with $\alpha = 0.05$) to adjust $P$ values to assess the predictive value of the proposed radiological analyser and routine clinicopathological risk factors in a specific risk group.

### Radiogenomic analysis for imaging-classified subtypes

As shown in Fig. 2, after identifying radiological clusters associated with varying survival benefits following adjuvant chemotherapy, we further conducted an explainability analysis. To explore the underlying biology of radiological clusters, we used the RNA sequencing data from 60 patients in the training set to identify the enriched biological pathways associated with the imaging clusters. Differentially expressed genes in the two radiological subtypes were identified and gene set variation analysis (GSVA) was performed to compare the hallmark (v7.5.1) enrichment from MSigDB and Kyoto Encyclopedia of Genes and Genomes (KEGG) pathways in the radiological clusters.[17] We further assessed the tumour microenvironment (TME) and related immune and stromal components using a cellular deconvolution algorithm with the transcriptome.[18] Furthermore, we evaluated the benefits of fluorouracil-based chemotherapy and the underlying TME in patients with CRC using the GEO dataset.

### Pathologic correlations with imaging-classified subtypes

We further comprised quantitative pathologic patterns for imaging-classified phenotypes for biologically distinct CRC microenvironments. Relevant prognostic and predictive markers used routinely in the clinical management of CRC were extracted from histopathological reports. Glass slides from whole-tumour sections stained with haematoxylin-eosin (H&E) as part of routine pathological practice were also collected, and the patterns of haemorrhage, necrosis, tertiary lymphoid structure (TLS), germinal centre $^{+}$TLS (GC$^{+}$TLS), tumour budding, and desmoplastic reactions were evaluated by two pathologists specialising in gastrointestinal cancers. Difficult cases were discussed to obtain an expert consensus diagnosis.

Double immunohistochemistry (IHC) for CD31 and PanCK was performed on tumour tissue sections. Different blood vessel markers have been used to differentiate histologically defined vessel subsets.[19–21] CD31 was used as a pan-endothelial marker because it stains all vessel endothelial cells at different time points. CD34 is mainly found in vessel formation in the early and intermediate stages, whereas von Willebrand factor (vWF) primarily stains later-stage vessels. vWF immunoreactivity is predominantly detected in morphologically recognisable thin-walled veins and thick-walled arteries.[22] The tumour-stroma ratio (TSR) was automatically calculated using QuPath. The number of vessel junctions indicating the extent of branching, mean mesh size representing the lumen size, and the sum of the segment lengths were quantified using ImageJ software using the "Color Deconvolution" and "Angiogenesis Analyser" plugin tools (details in Supplementary Methods). As shown in Supplementary Figs. S2 and S3, the vessels were delimited with an outline.

Multiplex IHC (mIHC) was performed on two sequential CRC tissue sections to visualise vessel phenotypes and partial distribution of immune cells. Ten formalin-fixed, paraffin-embedded specimens were collected from patients with stage II CRC who underwent surgery at GDPH. Based on the radiogenomic analysis results and reviewed literature, a broad variety of potential antigens with available antibodies were screened for panel inclusion feasibility, and self-designed multiplex immunofluorescence panels concerning vasculature and immune cell infiltration were used. HALO image analysis software (v. 3.2; Indica Labs) was used to assess the infiltration of immune cells and conduct spatial analysis. Different blood vessel markers were used to differentiate the histologically defined vessel subsets.[19] The previously defined 1000 μm-wide tumoural interface areas[23] were segmented along the tumour margin into ten tiles, with each tile having a 100 μm-wide zone. The cell numbers in ten layers on both the stromal and tumoural sides of the interface were quantified. The distances between the immune cell components and the tumour margin in two bilateral directions along the border were also calculated.

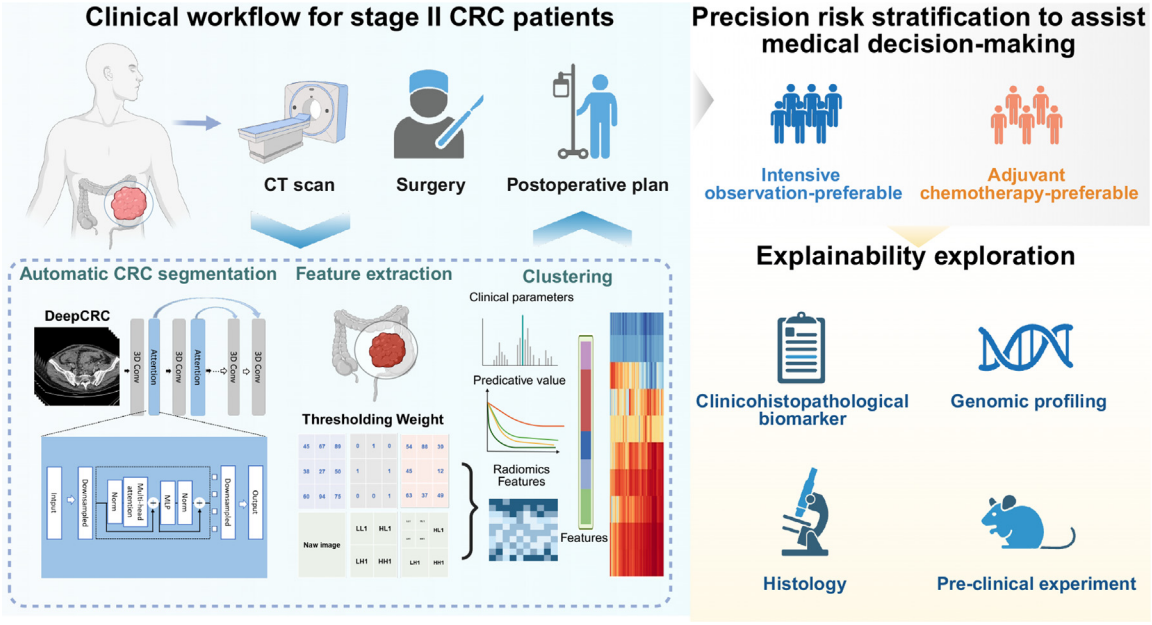


***Fig. 2:*** **The AI-driven risk stratification system of patients with stage II resected CRC**. Abbreviations: CRC, colorectal cancer. Created with BioRender.com.

### Intervention on the preclinical mouse model for observation of imaging features

We conducted a preclinical imaging experiment using mouse models to assess the correlation between the identified radiomics features and vascular patterns. A total of 12 female BALB/c mice (age: 4–6 weeks) were used in this study. All mice were housed in the same facility under controlled conditions (temperature: 22 °C, 12-h light/dark cycle). Cage locations were randomized across racks to minimize microenvironmental effects. CT26 cell-line derived xenograft (CDX) models were established to compare the vascular patterns in tumours using CT imaging features. Anlotinib, a multitarget antiangiogenic tyrosine kinase inhibitor, reported to significantly affect vascular patterns of sensitizing non-angiogenic tumours to chemotherapy,[24] was used for the modification of vascular patterns in mouse models. A single researcher (uninvolved in subsequent stages) randomly allocated mice to the anlotinib intervention group and saline control group using a block randomization protocol. Anlotinib was intragastrically administered to the mice in the intervention group (n = 6), and saline (n = 6) was spontaneously administered to the mice in the control group. Contrast-enhanced CT images were obtained from both groups using a micro-CT after a complete course of anlotinib treatment. Tumours were manually delineated, and radiomic features were extracted from the CT images. All mice were euthanized via cervical dislocation under anaesthesia (isoflurane 5%) at the study endpoint. Tumours were excised, fixed in 4% paraformaldehyde, and subjected to H&E and CD31/α-SMA-staining IHC for vascular pattern analysis. Normality of the vessels was measured using the microvessel pericyte coverage index (MPI). According to the preliminary experimental results, the mean and standard deviation of MPI in the experimental group and control group were 1.2 + 0.92 and 3.9 + 1.2. The sample size of this study was estimated using the PASS (Power Analysis and Sample Size) software (v15.0.5, NCSS). The sample size calculation formula of two-sample t-test was adopted, with a type I error (α) set at 0.05 (two-sided test) and a power of above 90% (corresponding to a type II error (β) of 0.1). The sample size of each group collected in this study met the minimum sample size requirement ($n \geq 10$). Pathologists analysing histology were blinded to treatment groups and imaging results. Mann-Whitney U tests were conducted on selected radiomics features in radiological risk stratification model to assess the statistical significance of variations in the values associated with different vascular patterns. No animals were excluded post-randomization. All mice completed the study protocol. The detailed analysis methods are described in the Supplementary Materials. The validated correlation was evaluated to assess the relationship between radiomic features and vessel normality in CRC, to support the clinical translation of radiomic features for optimizing chemotherapy delivery.

### Statistical analysis

Normality tests (Shapiro–Wilk test) were used to determine whether the distribution of the data. Fisher's exact test or the $\chi^2$ test were utilised for categorical

measurements; the Kruskal–Wallis or Mann–Whitney U tests were applied for continuous measurements. Feature robustness was tested using ICCs. The interaction term iHR between treatment and survival status was calculated using the Cox proportional hazards regression method for treatment-specific survival benefit.[16] Radiological clusters were clustered using unsupervised hierarchical clustering. Kaplan–Meier survival curves were constructed to assess the survival outcomes between the two radiological clusters, and the log-rank test was used to compare survival differences. Statistical significance was set at $P$ value of less than 0.05. All statistical analyses and graphical representations were performed using Python version 3.7.11 and R version 4.3.3.

### Role of funders

The funding agencies played no role in the study design, data collection, data analysis, data interpretation, or manuscript writing.

## Results

### Clinicopathological features of the cohorts

As shown in Fig. 1, six cohorts of patients with CRC were enrolled. The clinicopathological features of the patients are shown in Supplementary Tables S1 and S2. For model development and validation, 582 patients were enrolled in this study, including 405 in the primary training set from the GDPH, 153 from the YNCC, and 24 from the TCIA database for the two external test sets. The percentage of patients who received chemotherapy in the training and test sets was 52.6%, 38.6%, and 54.2%, respectively. The median follow-up times were 63.0 months (interquartile range, 55.0–72.0) in the primary cohort, 58.0 months (49.0–68.0) and 67.0 months (60.0–76.5) in the external cohorts. Furthermore, three more public datasets (GSE28702, GSE62080, and GSE69657) were collected as chemotherapy-associated datasets, including 70 non-responders and 64 responders to fluorouracil-based treatment.

### Radiological subtypes associated with chemotherapy survival benefits

The study design is illustrated in Fig. 2. A total of 851 radiomic features were extracted, and ten robust radiomic features (Supplementary Table S3, Supplementary Figs. S4 and S5) with significant treatment interaction effects were selected for consensus clustering to classify patients into AC-preferable and OO-preferable clusters (Fig. 3a). As shown in Supplementary Table S4, the average tumour volume was higher in the OO-preferable group, whereas tumour volume-related features were not predictive of treatment choices. Typical CRC images with different risk stratifications are shown in Fig. 3b. For AC-preferable patients, adjuvant chemotherapy significantly improved overall survival (overall survival (OS) in both the primary (P = 0.005, log-rank test) and validation cohorts (P = 0.010) (Fig. 3c). Adjuvant chemotherapy showed a trend toward improved disease-free survival (DFS) in both the primary cohort (P = 0.117, log-rank test) and the validation cohort (P = 0.342), but these did not reach statistical significance individually. When combining the cohorts, the interaction effect between radiological clusters and chemotherapy reached statistical significance [iHR 2.88 (1.01–8.25), $P_{interaction}$ = 0.048] (Supplementary Fig. S6). The same trend was observed in the TCIA dataset (Supplementary Fig. S7). As shown in Fig. 3d, based on radiological clustering, 109 (25.9%) patients in the primary cohort and 59 (38.6%) patients in the validation cohort were classified as AC-preferable, while 296 (73.1%) patients in the primary cohort and 94 (61.4%) patients in the validation cohort were classified as OO-preferable. These findings suggest a potentially substantial number of missed (25.5% in the primary cohort and 42.0% in the external cohort) and overtreated cases (71.8% and 69.9%, respectively) in current clinical practice.

We evaluated the efficacy of chemotherapy in relation to the proposed radiological risk stratification model and each high-risk factor identified from clinical and molecular records. As shown in Supplementary Table S5, the predictive power of the proposed radiological risk stratification model was statistically significant [iHR 5.35, (95% CI: 1.98, 14.41), adjusted $P_{interaction}$ = 0.001]. We further conducted for multiple comparisons to mitigate the risk of Type I errors for post-hoc analyses involving multiple markers across different subgroups. Specifically, the Benjamini-Hochberg FDR method (with $\alpha = 0.05$) were applied to assessing the predictive value of the proposed radiological analyser and routine clinicopathological risk factors in a specific risk group. The radiological risk analyzer-defined cluster remained a significant predictor (adjusted $P = 0.012$, Cox regression) for survival across all patients. However, it was not significant in the analyses after multiple comparisons correction for individual cohorts, with $P$ values ranging from 0.023 to 0.296 for the GDPH cohort and from 0.020 to 0.259 for the YNCC cohort. No other clinicohistopathological factors (sex, age, pT staging, histological grade, lymph node sampling, tumour location, differentiation, MMR status, or vascular/perineural invasion) demonstrated statistically significant prognostic value across cohorts (adjusted P > 0.05, Cox regression). We analysed the association between the radiological clustering subtypes and available clinicopathological risk factors at diagnosis in the primary cohort (Fig. 3e, Supplementary Table S6). In the AC-preferable group, there was a lower proportion of tumours in the rectum (4.8% vs. 25.6%) than that in the OO-preferable group. No other histopathological risk factors commonly used in clinical reports were found to correlate with radiological categorisation.

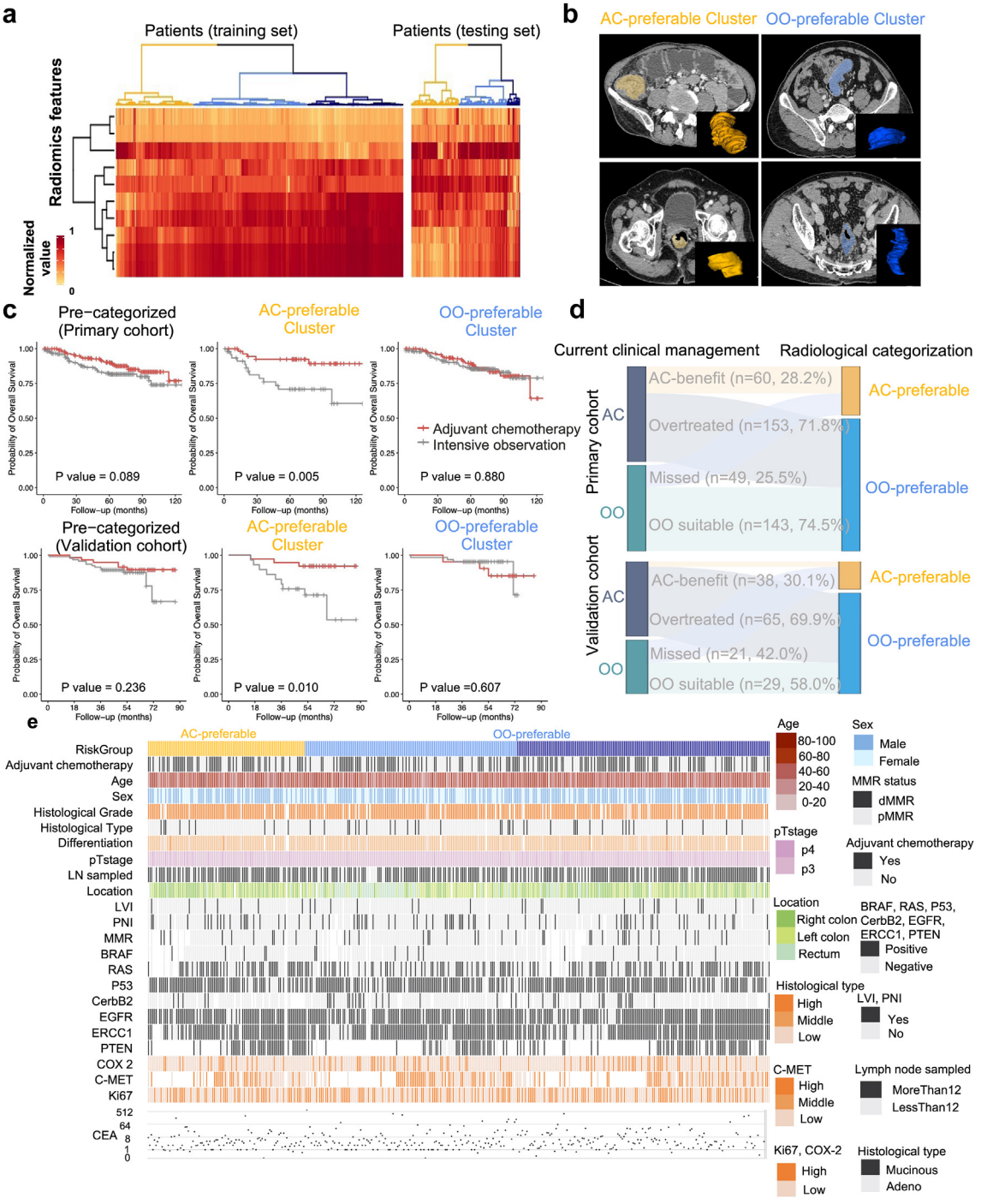


***Fig. 3*: Risk stratification of patients with stage II colorectal cancer**. (**a**) Heatmap plot of patients stratified by unsupervised clusters generated from radiomic features by-treatment interaction effects in the primary training set and validation set. (**b**) Example images from patients with CRC in different radiological clusters. (**c**) OS benefit stratification by radiological categorization. Kaplan–Meier estimates of OS for the pre-categorized groups and each subgroup by treatments in the primary (n = 405) and validation cohorts (n = 153). *P* values were derived from the log-rank test. (**d**) Diagram showing the proportion of patients who will receive different treatments according to the proposed method or current clinical management. (**e**) Clinicohistopathological features by different radiological clusters (n = 109 and n = 296). Abbreviations: CRC, colorectal cancer; OS, overall survival; AC, adjuvant chemotherapy; OO, observation only.

### Radiogenomic analysis revealed a significant difference in stromal abundance between AI-powered radiological clusters

Next, we conducted radiogenomic analysis to identify the biological rationales underlying the radiological clusters (Fig. 4a). Different biological pathways were identified between the radiological clusters. As shown in Fig. 4b and Supplementary Fig. S8, 397 differentially expressed genes were identified using the hallmark gene sets in the two radiological subtypes. The apical junction, Notch signalling, Hedgehog signalling, and myogenesis pathways were upregulated in the AC-preferable cluster. OO-preferable CRC was enriched in the E2F target, MYC target v1, MYC target v2, oxidative phosphorylation, and peroxisomal signalling pathways. The two radiological clusters demonstrated borderline significant differences in stromal infiltration, with the AC-preferable cluster having higher overall stromal infiltration than the OO-preferable cluster (Supplementary Fig. S9). Higher infiltration of immune and stromal cells in the AC-preferable group was also observed. As shown in Fig. 4c, the AC-preferable cluster had a higher immune

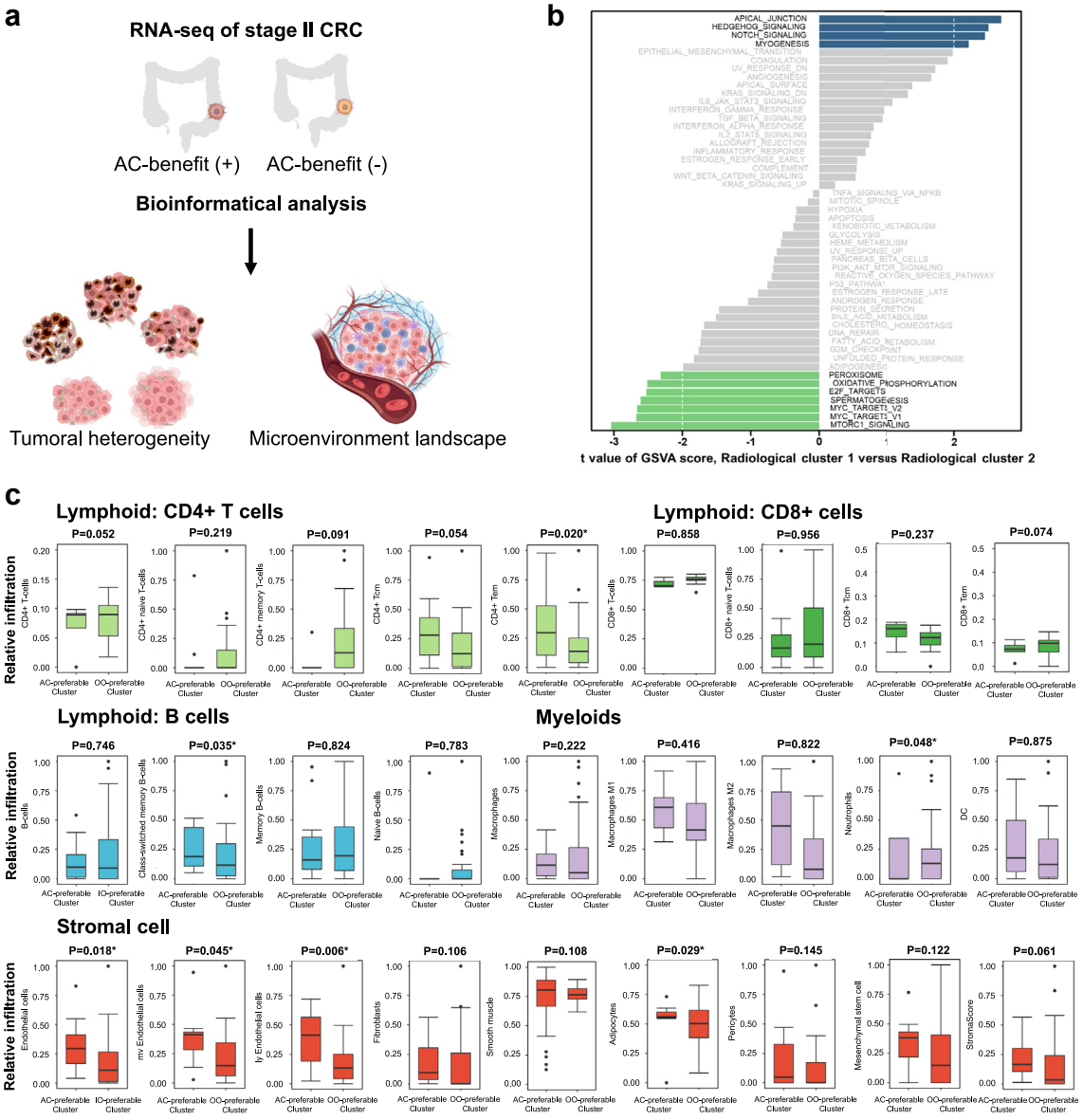


*Fig. 4:* **Radiogenomic analysis**. (**a**) Bioinformatics analysis illustration. (**b**) GSVA enrichment scores obtained for the up-regulated and down-regulated gene sets in the primary dataset (n = 60). (**c**) Boxplots of the fraction of immune and stromal cell infiltration by radiological clusters in the primary cohort (n = 60). *P* values were derived from the Mann–Whitney U test. Abbreviations: CRC, colorectal cancer; GSVA, gene set variation analysis; AC, adjuvant chemotherapy; OO, observation only.

cell distribution of $CD4^+$-T cells ($P$ = 0.020, Mann–Whitney U test) and class-switched memory B-cells ($P$ = 0.035). Infiltration of endothelial cells (ECs, $P$ = 0.018) was significantly higher in the AC-preferable cluster than in the OO-preferable cluster. We further assessed the benefits of chemotherapy using three validation datasets. The same trend of higher abundance of ECs in responders was observed for all three GSE datasets (GSE28702, GSE62080, and GSE69657). The infiltration of EC and microvascular EC was significantly higher in the responder group than that in the non-responder group in GSE28702, and the infiltration of EC was significantly higher in the GSE62080 responder group (Supplementary Fig. S10).

### Vascular pathomorphological distinctions and spatial-specific immune cell infiltration patterns in two radiological clusters

Different vessel histopathological patterns were observed between the radiological clusters. A total of 305 H&E-stained slides, 40 double-stained IHC slides from the primary cohort, and 111 H&E-stained slides from the validation cohort were obtained. Expert pathologists evaluated the immune and stromal infiltration-related histopathological patterns of CRC, including haemorrhage, necrosis, TLS, $GC^+$TLS, tumour budding, and desmoplastic reactions (Supplementary Fig. S11). As shown in Fig. 5a and b, we found a higher percentage of necrosis ($P$ = 0.049, $\chi^2$ test) and haemorrhage ($P$ = 0.044) in the OO-preferable cluster (Supplementary Table S7), which was validated in the external dataset (Supplementary Table S8). Compared to the AC-preferable cluster, the vessel structures in the tumoural area of the OO-preferable cluster were more disorganised and morphologically abnormal (Supplementary Table S9). As shown in Fig. 5c, in the OO-preferable cluster, the presence of bizarre vessels, exhibiting irregular branches in a chaotic network of tangles that crisscross the stroma, was more frequent ($P$ = 0.045, Mann–Whitney U tests). Branching vessels ($P$ = 0.035) was also more frequent, the mean mesh size representing the lumen size was greater and the size range (mean ± standard deviation: 6276 ± 2875 vs. 4561 ± 1333 pixels, $P$ = 0.016) was wider in the OO-preferable cluster, indicating that vessel diameters were uneven with some being oversized and some being immature smaller vessels. As shown in Fig. 5d, a significantly higher TSR, indicating a higher proportion of stroma in the tumour area, was found in the AC-preferable cluster than that in the OO-preferable cluster (mean: 0.484 vs. 0.389, $P$ = 0.014).

Further experiments revealed the heterogeneous morphology of the vasculature phenotypes and spatial immune and stromal infiltration. We found a significantly higher density of $NG2^+$ vessels ($P$ = 0.003, Mann–Whitney U tests) in the AC-preferable subtype than in the OO-preferable subtype, indicating a more structured lumen with adequate pericyte coverage (Fig. 5e). We found a higher density of $vWF^+$ vessels that were mainly expressed in the late stage ($P$ = 0.028), and a lower density of $CD34^+$ vessels that were mainly expressed at an early stage during vessel formation ($P$ = 0.032) in the AC-preferable subtype than in the OO-preferable subtype (Fig. 5f). The distribution of immune cells is shown in Fig. 5g. We found that the average distance between B cells and $CD4^+$-T cells was predominantly positive in the AC-preferable subtype, but negative in the OO-preferable subtype, indicating a significantly higher distribution of immune cells in the tumour area in the AC-preferable subtype ($P$ = 0.016) (Fig. 5h). As shown in Fig. 5i, immune cell spatial analysis at the interface showed more enriched infiltration of immune cells in layers closer to the margin in the AC-preferable subtype, indicating more abundant infiltration of B, $CD4^+$-T, and $CD8^+$-T cells in the core tumoural area than in the OO-preferable subtype (Supplementary Fig. S12).

### Preclinical imaging: correlation between radiological features and changes in vessel morphology

To verify the hypothesis that interventions in vessel morphology could influence image-derived radiomic features, we conducted a preclinical experiment using mouse models of CRC (Fig. 6a). Tumour growth was significantly inhibited in the anlotinib-treated group compared to the control group (Fig. 6b, Supplementary Fig. S13). We evaluated the features from CT images of the mouse model (Fig. 6c). The vascular morphology (visualised proportion of pericyte-covered blood vessels by CD31 and α-SMA immunostaining) increased after anlotinib treatment, as compared with that of control group (Fig. 6d), suggesting that anlotinib could promote mature tumour vessels. Fig. 6e shows that eight of the ten selected predictors were significantly different between the control and treatment groups, indicating that these radiomic features were influenced by vessel morphology-related factors.

Our study explored multiscale tumoural heterogeneity at the radiological, pathological, and molecular gene levels to estimate malignant progression and treatment response, providing preclinical evidence for the change in vascular morphology in tumour stroma in the chemoresistance of CRC, which could be reflected from imaging features (Fig. 6f).

## Discussion

Accurate risk stratification is important for tailored selection of adjuvant chemotherapy and follow-up strategies in patients with heterogeneous stage II CRC.[25] Our proposed AI pipeline can be integrated into current clinical workflows and has significant application potential in hospitals for the promotion of precision medicine. A prognostic biomarker reflecting the intrinsic biology of a tumour could divide the population of patients into good or poor survival regardless of

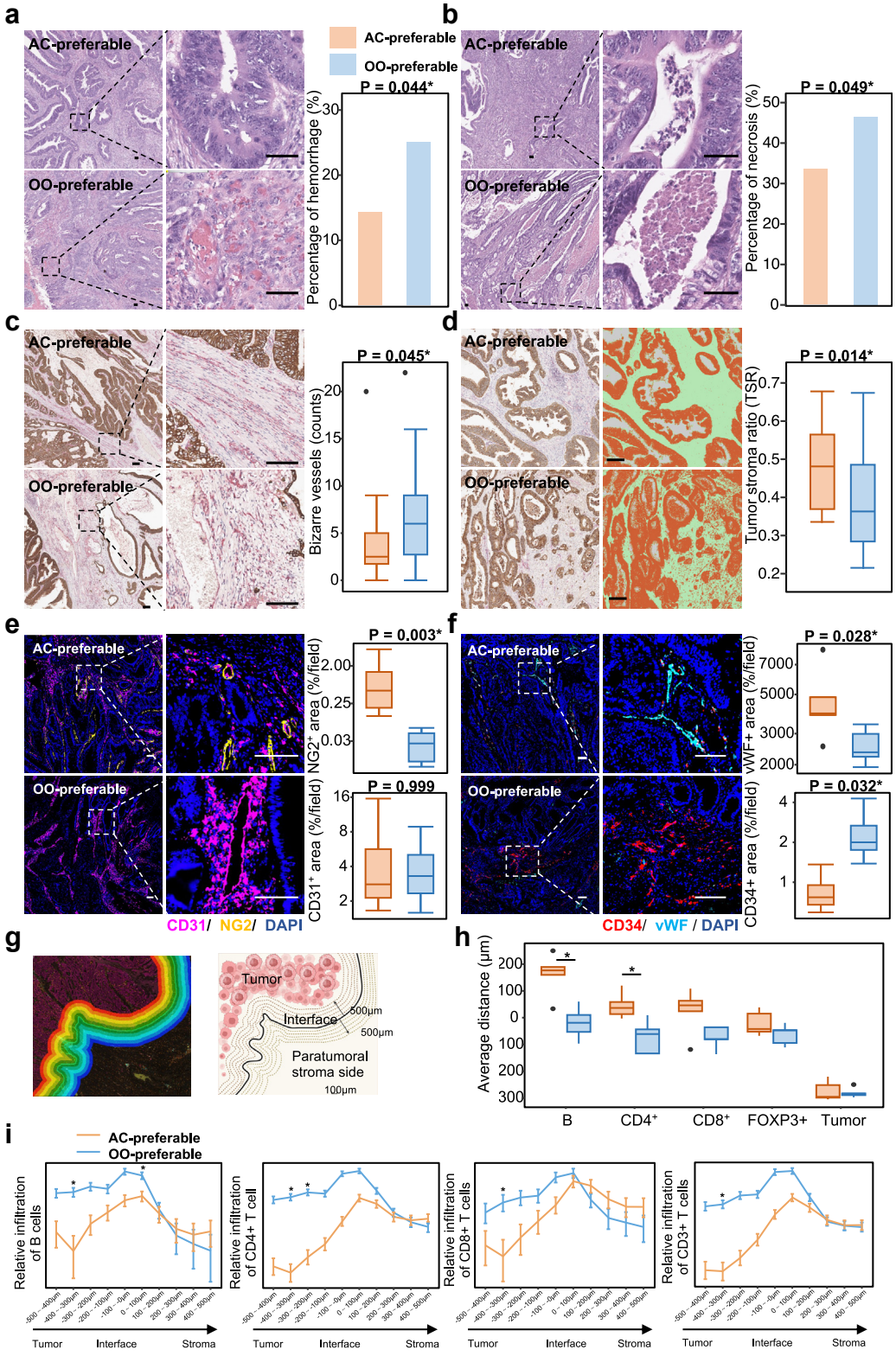


*Fig. 5:* **Histopathological analysis**. (**a**) Representative images of haemorrhage and the boxplot for percentage of haemorrhage from different radiological clusters (n = 305) in haematoxylin-eosin (H&E)-stained slides (40× and 100×, scale bar: 100 μm). *P* values were derived from the $\chi^2$

therapeutic schemes, while a predictive biomarker differentiates the relative efficacy of the two treatments in biomarker-positive patients from that for biomarker-negative patients.[26] In this study, we developed an automatic imaging-based tumour detection and risk stratification model incorporating treatment-by-biomarker interaction analysis for decision-making guidance regarding adjuvant therapy to improve the long-term survival of patients. Specifically, clinical translation was investigated through radiological clustering to stratify patients for chemotherapy regimens. These classifications suggest that current clinical practices may result in substantial misclassification, with 20%–40% potentially undertreated, and round 70% potentially overtreated. These findings highlight the potential of radiomic-based stratification to enhance precision in chemotherapy selection, reducing missed treatment opportunities and overtreatment, thereby improving therapeutic outcomes in colorectal cancer management. The results demonstrated that the AI-powered radiomic profiling analyser was predictive of treatment choice, independent of the molecular and clinicopathological features in the American National Comprehensive Cancer Network guideline.[3] The GDPH and YNCC cohorts exhibited demographic and clinicopathological differences; however, the AI-powered radiological risk stratification model demonstrated robust external validation across both cohorts. This validation highlights the tool's reliability in bridging disparities inherent in real-world clinical data, thereby strengthening its translational potential. Radiological stratification could potentially reduce the morbidity and economic costs associated with current stage II CRC management by avoiding overtreatment and identifying missed cases that are suitable for adjuvant treatment.

Interpretability remains a significant challenge in current AI research.[27] Tomaszewski et al.[28] have underscored the increasing momentum within the field to reintegrate biological significance into radiomics. In this study, we propose an approach for the integration of multimodal data to enhance the explainability of the AI model, which includes genomic correlates,[8,29,30] pathologic analyses[9–11,31] and the demonstration of a causal relationship.[12,13] Efforts have focused on elucidating the biological mechanisms and pathways that lead to the morphological and corresponding radiological variations. First, radiogenomic analysis highlighted a link between stromal EC infiltration and the survival benefit of chemotherapy in our local cohort and in the GEO databases. Furthermore, to close the knowledge gap between radiographic patterns and gene expression, we revisited stroma-related histopathological features on routine H&E slides. Patients in the OO-preferable cluster presented with a higher proportion of abnormal vessels in the tumours than those in the AC-preferable cluster. In contrast, the AC-preferable cluster was characterised by more organised vasculature features, indicating better vessel function and more sensitive response to chemotherapy. Finally, we used interventions in mouse models of vessel morphology to correlate with histopathological features that could result in the alteration of individual predictive imaging features in the AI pipelines. Our study demonstrated that underlying tumour heterogeneity could be decoded by establishing correlations between imaging features and underlying morphological and molecular attributes. Vessel morphology, including vessel size, shape, branching, and wall composition, directly influences how tissues appear on CT imaging. Recent studies have demonstrated the potential of quantitative tumour-associated vasculature radiomic biomarkers from contrast-enhanced CT/magnetic resonance images to characterise tumour treatment responses.[32,33] Chaotic tumour vasculature which can be reflected in contrast-enhanced images, plays an established role in fostering elevated textural heterogeneity.[34] Conversely, the evidence linking immune cell infiltration to imaging features remains indirect,[34,35] warranting further investigation. Vessel morphology and immune cell infiltration interact dynamically.[36,37] Further studies are required to eliminate how immune-vascular crosstalk shapes radiological phenotypes.

test. (**b**) Representative images of necrosis and the boxplot for necrosis from different radiological clusters (n = 305) in H&E-stained slides (40× and 100×, scale bar: 100 μm). *P* values were derived from the $\chi^2$ test. (**c**) Representative images of double immunostaining of CD31 (red) and PanCK (brown) (40× and 100×, scale bar: 100 μm) and the boxplot for number of branching points (counts/field) between different radiological clusters (n = 40). *P* values were derived from the Mann–Whitney U tests. (**d**) Representative matched IHC images and segmented images of tumour epithelium (brown), stroma (green) and background (grey) using the pixel classifier algorithm in QuPath (scale bar: 200 μm). The boxplot for tumour-stroma ratio (TSR) between different radiological clusters (n = 40). *P* values were derived from the Mann–Whitney U tests. (**e**) Representative images of CD31 (purple) and NG2 (yellow) expression and the boxplots for relative percentage of $NG2^+$ and $CD31^+$ area in the tumoral area of CRC samples between different radiological clusters (n = 10). *P* values were derived from the Mann–Whitney U tests. (**f**) Representative images of CD34 (red) and vWF (blue) expression from different radiological clusters and the boxplots for relative percentage of $CD34^+$ and $vWF^+$ area in the tumoral area of CRC samples between different radiological clusters (n = 10). *P* values were derived from the Mann–Whitney U tests. (**g**) The construction of the tumour border in margin regions. (**h**) The average distance to the interface among two radiological groups. (**i**) Line graphs showing the average fraction of immune cells and the different subsets (B cells and T cells) among two radiological groups (n = 10) in different layers around the border of tumour. *P* values were derived from the Mann–Whitney U tests. Abbreviations: AC, adjuvant chemotherapy; CRC, colorectal cancer; IO, intensive observation. Created with BioRender.com.

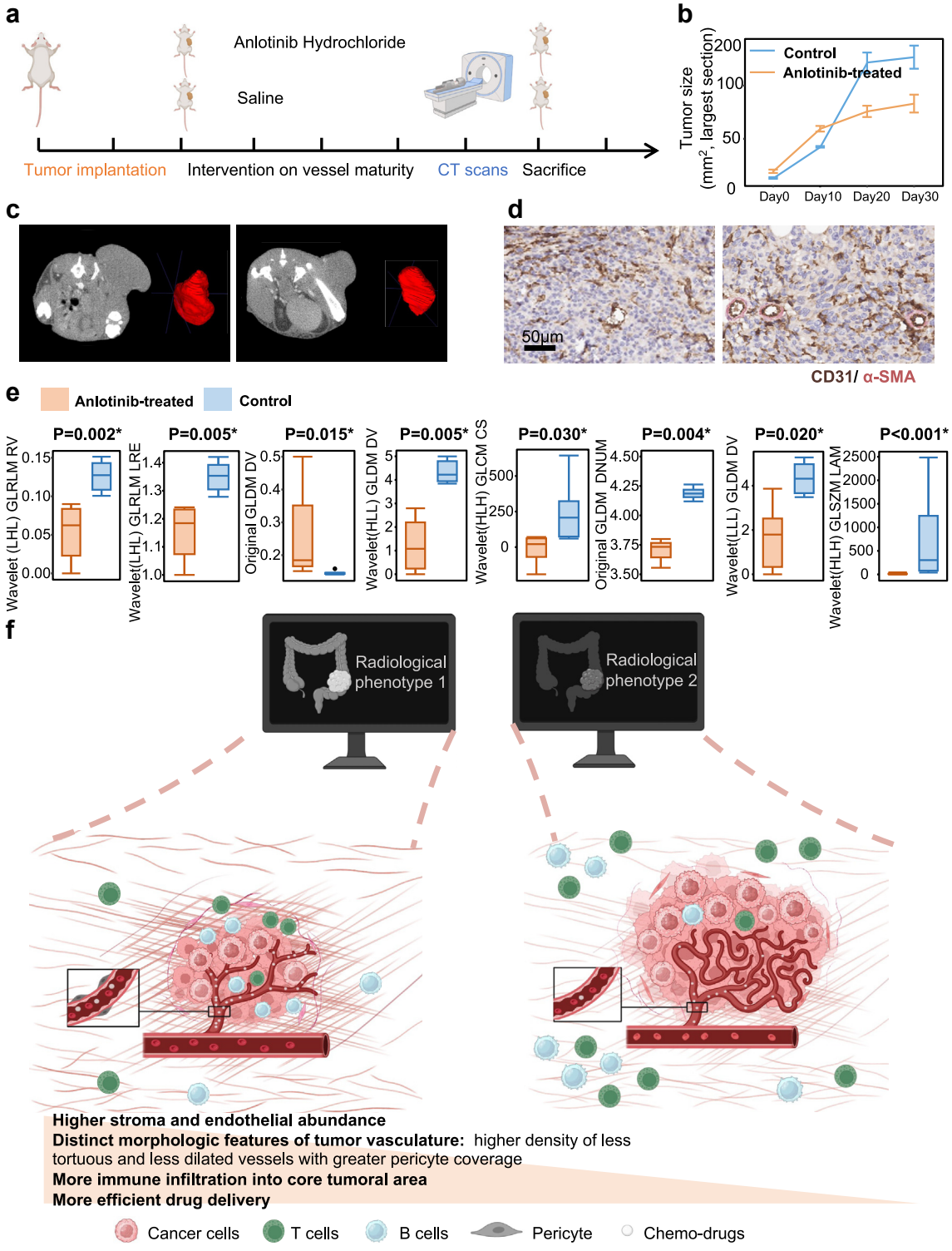


***Fig. 6:*** **Preclinical imaging analysis**. (**a**) Flowchart of vessel maturity treatment and CT imaging. (**b**) The growth curves for mouse models receiving no treatment (control) and anlotinib treatment. (**c**) Representative images of contrast-enhanced CT images for in control (left) and anlotinib-treated groups (right). (**d**) Immunofluorescent double staining for CD31 (endothelial marker, green) and α-SMA (vascular smooth muscle cell marker, red) of sections of tumour samples in control (left) and anlotinib-treated groups (right). (**e**) The eight selected radiomic features with significant differences in control (left, n = 6) and anlotinib-treated groups (right, n = 6). *P* values were derived from the Mann–Whitney U tests. (**f**) Schematic of the mechanisms by which heterogeneous morphology of tumour vessels in artificial intelligence-based radiological subtypes leads to different survival benefit from adjuvant chemotherapy for patients with stage II colorectal cancer. Abbreviations: α-SMA, a-smooth muscle actin. Created with BioRender.com.

We identified different radiological subtypes of stage II CRC and the proportion that could benefit from chemotherapy, which is potentially mediated by vascular morphology-related chemoresistance. Microvascular EC abundance has been reported to correlate with the number of mature blood vessels in the TME and is predictive of chemotherapy response and patient survival in CRC.[38] The OO-preferable cluster had a higher percentage of abnormal vessels than the AC-preferable cluster. Pathological blood vessels that are immature and not wrapped with pericytes do not function as normal blood vessels or efficiently deliver oxygen and drugs.[32] Improved vascular maturation and function allow more chemotherapeutic drugs to be delivered to the cancer.[39,40] Accumulating evidence indicates that EC heterogeneity can contribute to the TME and chemotherapy response.[41,42] Li et al.[39] reported CRC phenotypes responding poorly to chemotherapy could be sensitised to chemotherapeutic drugs by improving mature vasculature. The above-mentioned hypothesis agrees with the results of the present study, which indicates a close link between chemotherapy response and vasculature. Furthermore, the facilitation of mature vasculature has been reported to improve T cell abundance and boost the effectiveness of chemotherapy.[43] In this study, we also observed a significant enrichment of T and B cells on the tumour side of the border compared to the stromal side, which is in line with the known functions of these immune cell types in CRC and other types of cancer.[44,45] Tian et al.[46] reported $CD4^+$-T cells mediated vessel normalisation after immunotherapy and tumour vascular normalisation could mutually improve immunostimulation. Yan et al.[47] have demonstrated that tumour vascular structure is correlated with the regulation of $CD8^+$-T cells. Our results further suggest that tumour vasculature interacts with the fraction and function of immune cells in CRC.

There are some important limitations to the present study. First and foremost, while the analysis incorporated six independent cohorts to assess generalizability, key findings exhibited variability across cohorts after rigorous statistical correction. This remains a proof-of-concept study and should be interpreted with caution. First, the results demonstrate a robust benefit of adjuvant chemotherapy on OS in AC-preferable patients, but adjuvant chemotherapy showed a non-significant association with improved DFS. The nonsignificant P values may reflect limited power or a true absence of effect. An alternative explanation is that the differential impact of biomarkers on OS vs. DFS could possibly suggest that the current risk stratification may reflect systemic patient vulnerability rather than intrinsic tumor aggressiveness of CRC. This pattern indicates the need for replication in larger cohorts to explore potential effects. Second, although the pooled cohort analysis retained statistical significance, the lack of significance after multiple comparison correction was noted. These findings also underscore the need for prospective validation in larger, multicenter cohorts to confirm clinical utility. Second, there were inadequate clinical and molecular profiles in the public image resources, and some potential associations between imaging features and certain risk factors may have been concealed. Vascular endothelial growth factor-related signalling pathways play an important role in blood vessel growth; however, previous studies[48,49] have also revealed additional signalling moieties capable of stimulating and modulating angiogenesis. In this study, the inferred biological role of the vessel phenotypes was putative, requiring substantial experiments *in vivo* and *in vitro* to elucidate the causative and contributory factors related to the discovered angiogenic vessel phenotypes in future studies. Furthermore, there is an imaging difference between humans and mice, although we determined the comparison using unsupervised clustering algorithms to minimise the research gap, which is recommended where the imaging properties are highly heterogeneous. Finally, the sample size of the radiogenomic analysis was suboptimal, as it was difficult to collect multimodal data with a sufficient follow-up period. Although we further evaluated the benefits of fluorouracil-based chemotherapy and the underlying TME using the public GEO dataset to validate the radiogenomic findings, future large-scale, multimodal studies are anticipated to validate and expand these findings.

In summary, the proposed explainable AI-based imaging stratification model is a promising tool for optimising personalised decision making for patients with stage II CRC. These results can be further explored in basic and translational studies to identify the regulation and manipulation of cancer–microenvironment interactions that alter the course of cancer development, progression, and therapy.

#### Contributors

Conceptualization: C.X., Z.N., Y.H., Q.Z., and ZY.L.; Methodology C.X., Z.N., and ZY.L.; Project administration: C.L., Q.Z., and ZY.L.; Data curation: Y.H., G.T., C.L., ZH.L., X.C., J.C., K.Z., Q.Z., and ZY.L.; Formal analysis and data verification: C.X., Z.N., G.T., X.C., L.Y., W.H., S.L., and ZY.L.; Supervision: X.B., Y.H., C.L. and Q.Z.; Writing—original draft: C.X., C.L., Q.Z., and ZY.L.; Writing—review & editing: all authors. All authors read and approved the final version of the manuscript.

#### Data sharing statement

All data supporting the results of this study are available from the corresponding author upon request. The source data are provided in this study. The code used for the implementation of DeepCRC depends on the internal tooling and infrastructure, is under patent protection (application number: CN 202211260255.2), and thus cannot be publicly released. The major components of the DeepCRC automatic segmentation and radiomic feature extraction are available in open-source repositories: PyTorch (https://pytorch.org/); nnUNet (https://github.com/MIC-DKFZ/nnUNet) and PyRadiomics (https://pyradiomics.readthedocs.io/en/latest/). The public data (TCGA-CRC, GSE28702, GSE62080, and GSE69657) used in this study were acquired from the TCGA Research Network portal (https://portal.gdc.cancer.gov/), TCIA Imaging Archive (https://com/cancerimagingarchive.net), and Gene

Expression Omnibus (GEO, http://www.ncbi.nlm.nih.gov/geo/). The custom R script and radiomics data used in this study to train the predictive models were deposited in the GitHub repository available at https://github.com/cx601/AIRCSA. The gene expression data reported in this paper have been deposited in the OMIX, China National Center for Bioinformation/Beijing Institute of Genomics, Chinese Academy of Sciences (https://ngdc.cncb.ac.cn/omix: accession no. OMIX002301) and can be accessed at https://bigd.big.ac.cn/gsa-human/browse/HRA007581 for the FASTQ files.

#### Declaration of interests

We declare no competing interests.

#### Acknowledgements

The authors would like to acknowledge Prof. Yifang Ping from the Institute of Pathology and Southwest Cancer Centre, Third Military Medical University, and Dr. Xue Bai from the Department of Radiation Oncology, Southern Medical University, for helpful discussions. This work was funded by the National Science Fund of China (81925023, 82302299, and U22A2034), Guangdong Provincial Key Laboratory of Artificial Intelligence in Medical Image Analysis and Application (2022B1212010011), and High-level Hospital Construction Project (DFJHBF202105 and YKY-KF202204).

#### Appendix A. Supplementary data

Supplementary data related to this article can be found at https://doi.org/10.1016/j.ebiom.2025.105789.

#### References

1 Iveson TJ, Sobrero AF, Yoshino T, et al. Duration of adjuvant doublet chemotherapy (3 or 6 months) in patients with high-risk stage II colorectal cancer. *J Clin Oncol*. 2021;39(6):631–641.
2 Verhoeff SR, van Erning FN, Lemmens VE, de Wilt JH, Pruijt JF. Adjuvant chemotherapy is not associated with improved survival for all high-risk factors in stage II colon cancer. *Int J Cancer*. 2016;139(1):187–193.
3 Benson AB, Venook AP, Al-Hawary MM, et al. Colon cancer, version 2.2021, NCCN clinical practice guidelines in oncology. *J Natl Compr Canc Netw*. 2021;19(3):329–359.
4 Argilés G, Tabernero J, Labianca R, et al. Localised colon cancer: ESMO Clinical Practice Guidelines for diagnosis, treatment and follow-up. *Ann Oncol*. 2020;31(10):1291–1305.
5 Kleppe A, Skrede OJ, De Raedt S, et al. A clinical decision support system optimising adjuvant chemotherapy for colorectal cancers by integrating deep learning and pathological staging markers: a development and validation study. *Lancet Oncol*. 2022;23(9):1221–1232.
6 Huang YQ, Liang CH, He L, et al. Development and validation of a radiomics nomogram for preoperative prediction of lymph node metastasis in colorectal cancer. *J Clin Oncol*. 2016;34(18):2157–2164.
7 Guiot J, Vaidyanathan A, Deprez L, et al. A review in radiomics: making personalized medicine a reality via routine imaging. *Med Res Rev*. 2022;42(1):426–440.
8 Fan M, Xia P, Clarke R, Wang Y, Li L. Radiogenomic signatures reveal multiscale intratumour heterogeneity associated with biological functions and survival in breast cancer. *Nat Commun*. 2020;11(1):4861.
9 Nam JG, Park S, Park CM, et al. Histopathologic basis for a chest CT deep learning survival prediction model in patients with lung adenocarcinoma. *Radiology*. 2022;305(2):441–451.
10 McGarry SD, Hurrell SL, Iczkowski KA, et al. Radio-pathomic maps of epithelium and lumen density predict the location of high-grade prostate cancer. *Int J Radiat Oncol Biol Phys*. 2018;101(5):1179–1187.
11 Jardim-Perassi BV, Huang S, Dominguez-Viqueira W, et al. Multiparametric MRI and coregistered histology identify tumor habitats in breast cancer mouse models. *Cancer Res*. 2019;79(15):3952–3964.
12 Panth KM, Leijenaar RT, Carvalho S, et al. Is there a causal relationship between genetic changes and radiomics-based image features? An in vivo preclinical experiment with doxycycline inducible GADD34 tumor cells. *Radiother Oncol*. 2015;116(3):462–466.
13 Zinn PO, Singh SK, Kotrotsou A, et al. A coclinical radiogenomic validation study: conserved magnetic resonance radiomic appearance of periostin-expressing glioblastoma in patients and xenograft models. *Clin Cancer Res*. 2018;24(24):6288–6299.
14 Yao L, Xia Y, Zhang H, et al. *DeepCRC: colorectum and colorectal cancer segmentation in CT scans via deep colorectal coordinate transform. International conference on medical image computing and computer-assisted intervention; 2022*. Springer; 2022:564–573.
15 van Griethuysen JJM, Fedorov A, Parmar C, et al. Computational radiomics system to decode the radiographic phenotype. *Cancer Res*. 2017;77(21):e104–e107.
16 Liu SY, Bao H, Wang Q, et al. Genomic signatures define three subtypes of EGFR-mutant stage II-III non-small-cell lung cancer with distinct adjuvant therapy outcomes. *Nat Commun*. 2021;12(1):6450.
17 Hänzelmann S, Castelo R, Guinney J. GSVA: gene set variation analysis for microarray and RNA-Seq data. *BMC Bioinformatics*. 2013;14(1):7.
18 Aran D, Hu Z, Butte AJ. xCell: digitally portraying the tissue cellular heterogeneity landscape. *Genome Biol*. 2017;18(1):220.
19 Uhlik MT, Liu J, Falcon BL, et al. Stromal-based signatures for the classification of gastric cancer. *Cancer Res*. 2016;76(9):2573–2586.
20 Eberhard A, Kahlert S, Goede V, Hemmerlein B, Plate KH, Augustin HG. Heterogeneity of angiogenesis and blood vessel maturation in human tumors: implications for antiangiogenic tumor therapies. *Cancer Res*. 2000;60(5):1388–1393.
21 Seo Y-S, Ko IO, Park H, et al. Radiation-Induced changes in tumor vessels and microenvironment contribute to therapeutic resistance in glioblastoma. *Front Oncol*. 2019;9:1259.
22 Goveia J, Rohlenova K, Taverna F, et al. An integrated gene expression landscape profiling approach to identify lung tumor endothelial cell heterogeneity and angiogenic candidates. *Cancer Cell*. 2020;37(1):21–36.e13.
23 Ji AL, Rubin AJ, Thrane K, et al. Multimodal analysis of composition and spatial architecture in human squamous cell carcinoma. *Cell*. 2020;182(2):497–514.e22.
24 Su Y, Luo B, Lu Y, et al. Anlotinib induces a T cell-inflamed tumor microenvironment by facilitating vessel normalization and enhances the efficacy of PD-1 checkpoint blockade in neuroblastoma. *Clin Cancer Res*. 2022;28(4):793–809.
25 Tie J, Cohen JD, Lahouel K, et al. Circulating tumor DNA analysis guiding adjuvant therapy in stage II colon cancer. *N Engl J Med*. 2022;386(24):2261–2272.
26 Ballman KV. Biomarker: predictive or prognostic? *J Clin Oncol*. 2015;33(33):3968–3971.
27 Ghassemi M, Oakden-Rayner L, Beam AL. The false hope of current approaches to explainable artificial intelligence in health care. *Lancet Digit Health*. 2021;3(11):e745–e750.
28 Tomaszewski MR, Gillies RJ. The biological meaning of radiomic features. *Radiology*. 2021;298(3):505–516.
29 Jiang L, You C, Xiao Y, et al. Radiogenomic analysis reveals tumor heterogeneity of triple-negative breast cancer. *Cell Rep Med*. 2022;3(7):100694.
30 Udayakumar D, Zhang Z, Xi Y, et al. Deciphering intratumoral molecular heterogeneity in clear cell renal cell carcinoma with a radiogenomics platform. *Clin Cancer Res*. 2021;27(17):4794–4806.
31 Bobholz SA, Lowman AK, Barrington A, et al. Radiomic features of multiparametric MRI present stable associations with analogous histological features in patients with brain cancer. *Tomography*. 2020;6(2):160–169.
32 Vaidya P, Bera K, Patil PD, et al. Novel, non-invasive imaging approach to identify patients with advanced non-small cell lung cancer at risk of hyperprogressive disease with immune checkpoint blockade. *J Immunother Cancer*. 2020;8(2):e001343.
33 Braman N, Prasanna P, Bera K, et al. Novel radiomic measurements of tumor-associated vasculature morphology on clinical imaging as a biomarker of treatment response in multiple cancers. *Clin Cancer Res*. 2022;28(20):4410–4424.
34 Koay EJ, Lee Y, Cristini V, et al. A visually apparent and quantifiable CT imaging feature identifies biophysical subtypes of pancreatic ductal adenocarcinoma. *Clin Cancer Res*. 2018;24(23):5883–5894.
35 Jiang X, Dudzinski S, Beckermann KE, et al. MRI of tumor T cell infiltration in response to checkpoint inhibitor therapy. *J Immunother Cancer*. 2020;8(1):e000328.
36 Asrir A, Tardiveau C, Coudert J, et al. Tumor-associated high endothelial venules mediate lymphocyte entry into tumors and predict response to PD-1 plus CTLA-4 combination immunotherapy. *Cancer Cell*. 2022;40(3):318–334.e9.

37 Schumacher TN, Thommen DS. Tertiary lymphoid structures in cancer. *Science*. 2022;375(6576):eabf9419.
38 Oshi M, Huyser MR, Le L, et al. Abundance of microvascular endothelial cells is associated with response to chemotherapy and prognosis in colorectal cancer. *Cancers (Basel)*. 2021;13(6):1477.
39 Li G-Y, Zhang S-J, Xue D, et al. Overcoming chemoresistance in non-angiogenic colorectal cancer by metformin via inhibiting endothelial apoptosis and vascular immaturity. *J Pharm Anal*. 2023;13(3):262–275.
40 Maes H, Kuchnio A, Peric A, et al. Tumor vessel normalization by chloroquine independent of autophagy. *Cancer Cell*. 2014;26(2):190–206.
41 Geldhof V, de Rooij L, Sokol L, et al. Single cell atlas identifies lipid-processing and immunomodulatory endothelial cells in healthy and malignant breast. *Nat Commun*. 2022;13(1):5511.
42 Strilic B, Yang L, Albarrán-Juárez J, et al. Tumour-cell-induced endothelial cell necroptosis via death receptor 6 promotes metastasis. *Nature*. 2016;536(7615):215–218.
43 Palucka AK, Coussens LM. The basis of oncoimmunology. *Cell*. 2016;164(6):1233–1247.
44 Pagès F, Mlecnik B, Marliot F, et al. International validation of the consensus Immunoscore for the classification of colon cancer: a prognostic and accuracy study. *Lancet*. 2018;391(10135):2128–2139.
45 Kuwahara T, Hazama S, Suzuki N, et al. Intratumoural-infiltrating CD4 + and FOXP3 + T cells as strong positive predictive markers for the prognosis of resectable colorectal cancer. *Br J Cancer*. 2019;121(8):659–665.
46 Tian L, Goldstein A, Wang H, et al. Mutual regulation of tumour vessel normalization and immunostimulatory reprogramming. *Nature*. 2017;544(7649):250–254.
47 Yan W, Qiu L, Yang M, et al. CXCL10 mediates CD8(+) T cells to facilitate vessel normalization and improve the efficacy of cetuximab combined with PD-1 checkpoint inhibitors in colorectal cancer. *Cancer Lett*. 2023;567:216263.
48 Bergers G, Hanahan D. Modes of resistance to anti-angiogenic therapy. *Nat Rev Cancer*. 2008;8(8):592–603.
49 De Palma M, Biziato D, Petrova TV. Microenvironmental regulation of tumour angiogenesis. *Nat Rev Cancer*. 2017;17(8):457–474.